nature photonics

Article

https://doi.org/10.1038/s41566-022-01110-y

Integrated passive nonlinear optical isolators

Received: 13 June 2022

Accepted: 16 October 2022

Published online: 01 December 2022

Check for updates

Alexander D. White [1,3] ✉, Geun Ho Ahn[1,3] ✉, Kasper Van Gasse[1], Ki Youl Yang [1], Lin Chang [2], John E. Bowers [2] & Jelena Vučković [1]

Fibre and bulk optical isolators are widely used to stabilize laser cavities by preventing unwanted feedback. However, their integrated counterparts have been slow to be adopted. Although several strategies for on-chip optical isolation have been realized, these rely on either integration of magneto-optic materials or high-frequency modulation with acousto-optic or electro-optic modulators. Here we demonstrate an integrated approach for passively isolating a continuous-wave laser using the intrinsically non-reciprocal Kerr nonlinearity in ring resonators. Using silicon nitride as a model platform, we achieve single ring isolation of 17–23 dB with 1.8–5.5-dB insertion loss, and a cascaded ring isolation of 35 dB with 5-dB insertion loss. Employing these devices, we demonstrate hybrid integration and isolation with a semiconductor laser chip.

The effort to integrate high-performance optical systems on-chip has made tremendous progress in recent years. Advances in ultra-low-loss photonic platforms[1], nonlinear photonics[2] and heterogeneous material integration[1,3] have enabled fully integrated turnkey frequency-comb sources[1,4], on-chip lasers with hertz linewidth[5], terabits-per-second (Tbps) communications on-chip[6,7], on-chip optical amplifiers[8] and much more. Although these systems will continue to improve, a lack of integrated optical isolation limits their performance.

Optical isolators allow for the transmission of light in one direction while preventing transmission in the other. This non-reciprocal behaviour is critical in optical systems in order to stabilize lasers and reduce noise by preventing unwanted back-reflection[9]. In traditional fibre and bulk optical systems, non-reciprocal transmission is achieved by the use of Faraday-effect-induced non-reciprocal polarization rotation under an external magnetic field[9–11]. This approach can be replicated on-chip by integrating magneto-optic materials into waveguides[10]. However, the scalability of the approach remains a substantial challenge due to the required custom material fabrication and lack of complementary metal–oxide–semiconductor (CMOS) compatibility. Furthermore, magneto-optic materials require a very strong magnet for their operation due to their weak effects in the visible to near-infrared (NIR) wavelength range[12,13] and are therefore difficult to operate in an integrated platform.

More recently, there has been remarkable progress in integrating magnet-free isolators using an active drive to break reciprocity. This drive has taken the form of a synthetic magnet[14,15], stimulated Brillouin scattering[16,17] and spatio-temporal modulation[18–20]. However, the requirement for an external drive increases the system complexity, often requires additional fabrication, and consumes power. Additionally, high-power radiofrequency drives contribute large amounts of electromagnetic background that can interfere with the sensitive electronics and photodetection in photonic integrated circuits. This poses inevitable challenges to the scalability and adoption of such devices. Therefore, to maximize the scalability and integration into current photonic integrated circuits, an ideal isolator would be fully passive and magnet-free.

Optical nonlinearity is a promising path towards breaking reciprocity[21–25], and is inherently present in most widely utilized photonic platforms, such as silicon nitride[2,26], silicon[22], gallium phosphide[27], tantala[28], silicon carbide[29,30] and lithium niobate[31,32]. Unfortunately, due to dynamic reciprocity, many proposals for non-reciprocal transmission using optical nonlinearities cannot function as isolators[33]. However, by carefully choosing the mode of operation, isolation using optical nonlinearity is possible and has been demonstrated with discrete components[24].

In this Article we demonstrate integrated continuous-wave isolators using the Kerr effect present in thin-film silicon-nitride ring resonators. The Kerr effect breaks the degeneracy between the clockwise and counterclockwise modes of the ring and allows for nonreciprocal

[1]E. L. Ginzton Laboratory, Stanford University, Stanford, CA, USA. [2]Department of Electrical and Computer Engineering, University of California, Santa Barbara, CA, USA. [3]These authors contributed equally: Alexander D. White, Geun Ho Ahn. ✉e-mail: adwhite@stanford.edu; gahn@stanford.edu

https://doi.org/10.1038/s41566-022-01110-y

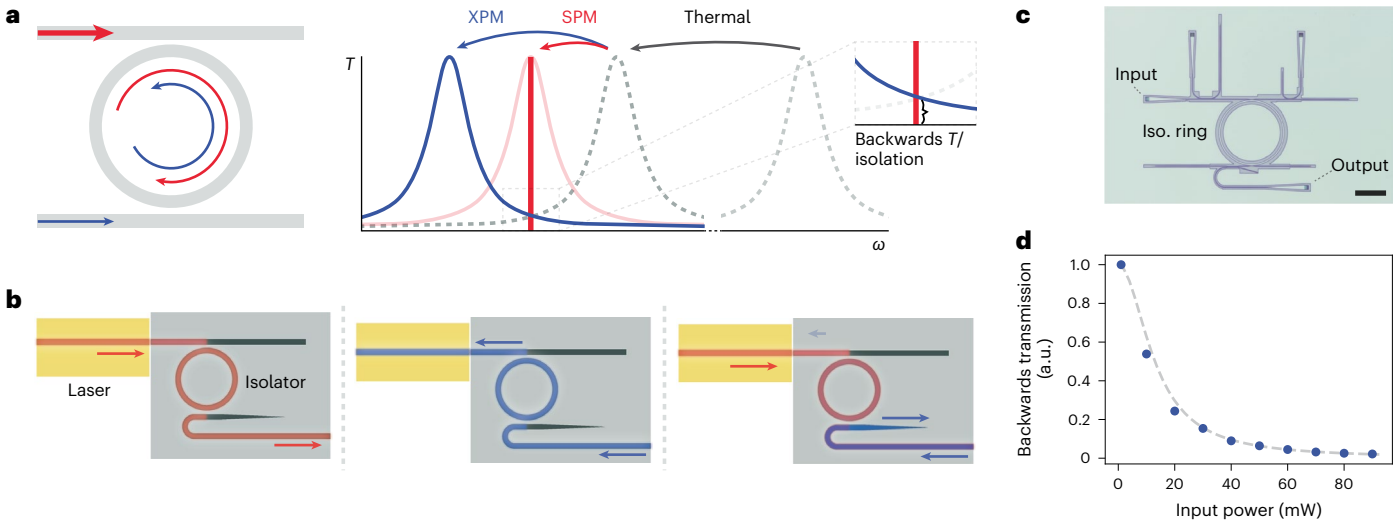

Fig. 1 | Theory of operation. a, Schematic showing the operation principle of the integrated nonlinear optical isolators. Plot shows transmission (T) vs. frequency (ω). **b**, Illustration of the isolator coupled directly to the laser that drives it, in the presence of the laser only (red), unwanted backward transmission only (blue) and the laser with backward transmission. When the laser is on, the backward transmission is no longer resonant and the laser is isolated. **c**, Image of a silicon-nitride device. Scale bar, 100 μm. **d**, Theoretical (dashed line) and experimental (blue data points) backwards transmission with varied input pump power and at maximum pump detuning, illustrating the Lorentzian transmission shape.

transmission. These devices are fully passive and require no input besides the laser that is being isolated. As such, the only power overhead is the small insertion loss from coupling of the ring resonator. Additionally, many integrated optical systems that would benefit from isolators already have high-quality silicon-nitride or commensurate components and could easily integrate this type of isolator with CMOS-compatible fabrication[1].

By varying the coupling of the ring resonators we can trade off insertion loss and isolation. As two examples, we demonstrate devices with a peak isolation of 23 dB with 4.6-dB insertion loss and isolation of 17 dB with a 1.3-dB insertion loss with 90 mW of optical power. As we are using an integrated photonics platform, we can reproducibly fabricate and cascade multiple isolators on the same chip, allowing us to demonstrate two cascaded isolators with an overall isolation ratio of 35 dB. Finally, we butt-couple a semiconductor laser-diode chip to the silicon-nitride isolators and demonstrate optical isolation in a system on a chip.

Theory of operation

The Kerr effect is the change in refractive index of a material due to its third-order nonlinearity in susceptibility, $\chi^{(3)}$. In the presence of two electric fields, the nonlinear polarization corresponding to this term is given by $P^{(3)}(t) = \epsilon_0\chi^{(3)}(E_1e^{-i\omega_1 t} + E_2e^{-i\omega_2 t} + \text{c.c.})^3$. Expanding this polynomial and keeping only the terms with the same frequencies, we find that $P^{(3)}(\omega_1) = 3\epsilon_0\chi^{(3)}(|E_1|^2 + 2|E_2|^2)E_1e^{-i\omega_1 t}$ and $P^{(3)}(\omega_2) = 3\epsilon_0\chi^{(3)}(2|E_1|^2 + |E_2|^2)E_2e^{-i\omega_1 t}$. Thus, there is an effective increase in the refractive index proportional to the optical intensity. Critically, the index change differs by a factor of two depending on the source of the optical power. The field that is degenerate with the mode under consideration contributes a refractive index increase of $3\epsilon_0\chi^{(3)}|E|^2$, self-phase modulation (SPM). The field that is non-degenerate contributes a refractive index increase of $6\epsilon_0\chi^{(3)}|E|^2$, cross-phase modulation (XPM). This difference provides an intrinsic non-reciprocity. If a strong pump beam is sent through a waveguide, and a weak probe is sent through in the other direction, the probe will accrue an additional phase shift due to the Kerr effect that is twice that of the pump.

We can apply the same principle to construct an isolator. Consider the set-up shown in Fig. 1a. A strong pump (red) is sent through a ring resonator with degenerate clockwise and counterclockwise resonances. This pump heats the ring, leading to a reciprocal thermo-optic increase in refractive index and corresponding decrease in resonance frequency. Additionally, the high power in the ring leads to an SPM of the clockwise mode and an XPM of the counterclockwise mode. This shifts the resonance of the counterclockwise mode twice as far as the clockwise pump mode. The now split resonances allow for a near-unity transmission in the pump direction but substantially reduce the transmission at the same frequency in the reverse direction (blue). This reduction is represented by the Lorentzian lineshape of the cavity. Following ref. [24], we can calculate the expected isolation by combining this transmission reduction with the SPM resonance shift:

$$I = \frac{1}{1 + (2Q\frac{\Delta\omega}{\omega_0})^2}, \tag{1}$$

where the shift $\Delta\omega$ is given by

$$\Delta\omega = \omega_0\frac{n_2}{n}\frac{Q\lambda}{2\pi V_{\text{mode}}}\eta P_{\text{in}}, \tag{2}$$

where Q is the loaded quality factor of the ring, n_2 is the nonlinear refractive index, n is the linear refractive index, V_{mode} is the mode volume of the ring, and η is the coupling efficiency of the pump to the ring. We can characterize the power required for isolation by considering the input power required to isolate by 3 dB. We will refer to this power level as the isolation threshold, P_{thresh}, given by

$$P_{\text{thresh}} = \frac{n}{n_2}\frac{\pi V_{\text{mode}}}{Q^2\lambda\eta}. \tag{3}$$

This isolation is achieved solely by the intrinsic non-reciprocity of the ring, so no additional power is required for operation. Critically, the operation is unaffected by dynamic reciprocity. When a backwards-propagating signal is at the same frequency as the pump, dynamic reciprocity does not apply, and when a signal is at a different frequency from the pump, there is reciprocal but near-zero transmission (Supplementary Section 1). Additionally, it is important to note that this isolation ratio holds true not only for backwards-propagating

signals with powers that are small compared to the pump, but even for backwards signals commensurate to and stronger than the pump. When there is already pump power circulating in the ring, the backwards wave is not resonant with the cavity. Thus, the required input power to negate the mode splitting is in fact many times higher than the power of the pump[34,35].

Although the bandwidth of the isolation is limited by the resonance splitting, it is possible to add an additional linear filter that indefinitely extends the isolation bandwidth (Supplementary Section 2). Without this additional filter, the 3-dB bandwidth of the isolation can be given by

$$\omega_{3\mathrm{dB}} = 2\Delta\omega - \sqrt{2}\sqrt{\Delta\omega^2 - \frac{\omega_0^2}{4Q^2}}, \quad (4)$$

which is on the order of the linewidth of the cavity and grows as the isolation increases.

As this type of isolator requires continuous pump power (either with a continuous-wave pump or a pump that is pulsed at the ring free-spectral range), but no additional driving or modulation, it is ideal for directly isolating the output of a laser (Fig. 1b). The laser itself acts as the sole driver of isolation, and the device incurs no power consumption, losing power only to the small insertion loss from traversing the ring. There is no need for strong magnetic fields, active optical modulation or high-power radiofrequency drives, and device operation is not limited to a single photonic platform or wavelength range.

Device integration and measurement

As the isolation depends on Q^2, the mode volume, the nonlinear refractive index and the input power, it is critical to implement devices with a material that can support high-quality microresonators, has an appreciable $\chi^{(3)}$ and can handle very high optical intensities without incurring loss. Here we demonstrate integrated isolators using silicon nitride as a model system, as it has become one of the most prominent platforms for integrated nonlinear photonics[1].

We use thin-film silicon nitride (<400 nm), as it has the potential for CMOS integration compatibility given the lower film stress present[36,37]. In addition, the thin-silicon-nitride process allows for geometric dispersion properties that easily lead to a strong normal dispersion[37], allowing us to suppress spurious optical parametric oscillation (Supplementary Section 3). To maximize Q^2/V_{mode} while keeping the isolator compact, we use a ring diameter of 200 μm, as shown in Fig. 1c.

To measure the isolation of these devices, we use the pump–probe set-up shown in Fig. 2a. As the pump and probe are sourced from the same laser, they have the same optical frequency. For the first set of measurements, shown in Fig. 2b,c, the pump and probe wavelengths are scanned across the ring resonance. In Fig. 2d the pump is kept fixed. We send a high-power pump through the ring and simultaneously modulate and send a low-power probe through the ring in the opposite direction. We then scan the pump and probe across the resonance and read the reverse transmission using a lock-in amplifier. During the scan, the pump thermally pulls the ring until the ring unlocks at the peak of its resonance[38]. As the laser approaches the frequency of the ring, more optical power couples to the resonance. As a consequence of a small linear material absorption, this heats the ring and detunes the resonance further away from the laser. This continues until the laser frequency matches that of the resonance and is coupled maximally to the ring. Once the laser detunes past this point, the power in the ring begins to decrease, allowing the ring to cool and collapse back to the original resonance position. By monitoring the probe transmission at the resonance peak, we can obtain a direct measurement of the isolation (Supplementary Section 4). Additionally, by varying the pump power, we can measure the power-dependent isolation (Fig. 2b,c). As the pump power is increased, the peak isolation is redshifted and scales as a Lorentzian. We find excellent agreement between our measurements (Fig. 2b) and the expected transmission from a simple model of a thermally pulled ring with a Lorentzian power-dependent isolation (Fig. 2b, inset).

We also validate the operation of the isolator with a static pump frequency. The ring remains locked to the laser, and we can directly measure the backwards transmission of the device by sending optical pulses at the same frequency as the pump (Fig. 2d). Here, the resonator locking is initiated by tuning the laser frequency, but this can also be achieved by thermally tuning the ring (Supplementary Section 5). As the maximum transmission and isolation occur at the peak of the resonance, where the resonance can no longer follow the laser, locking can be disturbed by changes in ambient temperature. This can be alleviated through thermal stabilization of the ring[39]. However, the large thermal pulling allows ample overhead in laser detuning: for this device under 90-mW input power, a 1-GHz detuning from the unlocking point corresponds to only a 0.3-dB reduction in isolation and a 0.15-dB increase in insertion loss. Because of this, we are able to operate close to the maximum transmission without any temperature control of the photonic isolator chip and remain stably locked over the duration of the experiment.

Finally, we can measure the frequency response of the isolation by modulating the probe using an electro-optic modulator (EOM). This generates sidebands that we can sweep across the resonance. As only the redshifted sideband will be resonant with the redshifted backwards resonance, we can sweep the sideband frequency to map out the frequency response (Fig. 2e). We find, as expected from the XPM modulation, that the backward transmission has a Lorentzian profile detuned from the pump by the SPM resonance shift, $\Delta\omega$.

To maximize the performance of these isolators, it is important to consider both insertion loss and isolation. In this system, these are determined by the coupling rates to the two waveguides, κ_1 and κ_2, and the scattering rate of the ring into the environment, γ. Ideally, all power is transmitted into the ring, and all of the power in the ring is transmitted to the output port. This is made possible by increasing the ring coupling rates, but this has the effect of reducing the Q of the resonance and thus lowering the isolation. To maximize the isolation, the power must be transferred to the ring efficiently, but the coupling rates should be minimized to preserve the Q. This, of course, increases insertion loss. More precisely, the ring sees a power of $\frac{4\kappa_1(\kappa_2+\gamma)}{(\kappa_1+\kappa_2+\gamma)^2}$, the Q is impacted by a factor of $\frac{1}{\kappa_1+\kappa_2+\gamma}$, and the insertion loss is given by $\frac{4\kappa_1\kappa_2}{(\kappa_1+\kappa_2+\gamma)^2}$.

To interrogate this trade-off experimentally, we fabricated an array of 16 air-clad silicon-nitride isolators with varying coupling strengths and coupling asymmetries (Fig. 3b,c). We find these devices have an intrinsic quality factor of ~5 million (Supplementary Section 7). As expected, devices with weaker and more asymmetric coupling show higher isolation, but also higher insertion loss. We highlight the performance of two of the devices—a device with 1.8-dB insertion loss and an isolation threshold of 12.9 mW, and a device with 5.5-dB insertion loss and an isolation threshold of 6.5 mW (Fig. 3d). These devices show peak isolations at 90 mW of 16.6 dB and 23.4 dB, respectively.

As these isolators are integrated and can have low insertion loss, it is possible to fabricate and cascade multiple devices on the same chip, enabling an exponential enhancement in isolation (Fig. 4a). To test this, we fabricated two rings, the second slightly red-detuned from the first. This allows for the thermal shift to bring both rings onto resonance and lock them there. The isolation is maximized and overall insertion loss minimized at a given pump power when the second ring is red-detuned by a factor of the single ring insertion loss times the thermal pulling of the first ring (Supplementary Section 8). To characterize the isolation of cascaded rings, we first measure the power-dependent isolation of a single ring (Fig. 4c), using the same pump–probe measurement as described in Fig. 2a. We then repeat this measurement for two cascaded rings, one slightly red-detuned from the second. These results

https://doi.org/10.1038/s41566-022-01110-y

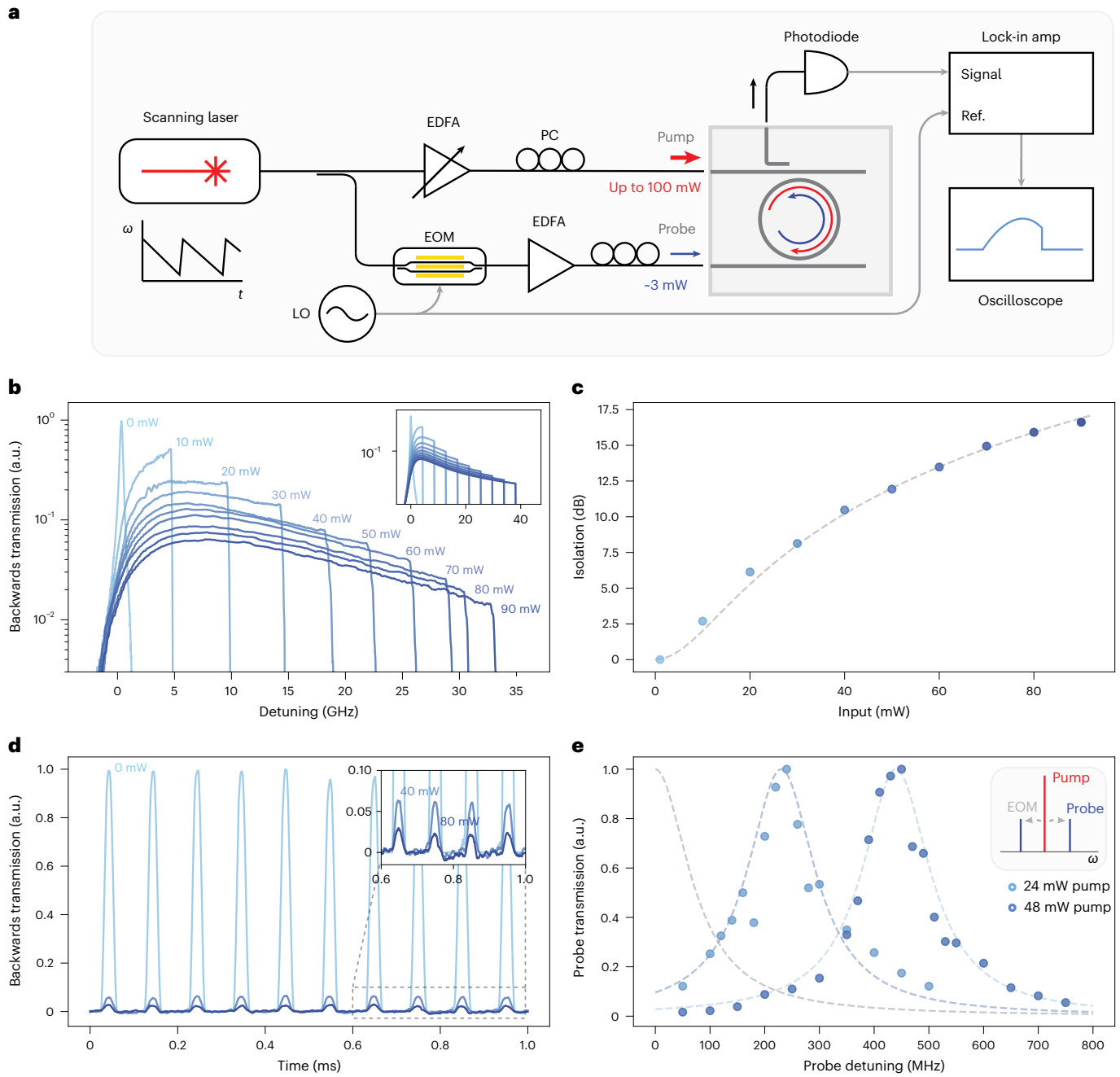

Fig. 2 | Isolation measurement. a, Schematic of the measurement set-up for characterizing the nonlinear optical isolators. EDFA, erbium-doped fibre amplifier; EOM, electro-optic modulator. PC, polarization controller; LO, 90-kHz electronic oscillator. **b**, Pump-power-dependent measurement of backwards transmission. Inset: theoretical pump power dependence. The line colours in the inset correspond to the colours in the main panel. **c**, Corresponding theoretical (dashed line) and experimental (blue data points) device isolation. Data-point colours correspond to the colours used in **b**. **d**, Pulsed backward transmission measurement with increasing pump power (0 mW, 40 mW, 80 mW). The inset shows a magnification of the section of the plot in the dashed box. **e**, Theoretical (dashed line) and experimental (blue data points) frequency dependence of the backwards transmission. Here, the probe is split into two sidebands with an EOM, and this sideband separation is swept with a frequency synthesizer. As expected, the backwards frequency response is shifted in proportion to the pump power.

are shown in Fig. 4d,e. The multiplicative effect of the cascaded rings enables us to achieve an isolation of 35 dB with an insertion loss of ~5 dB.

Finally, we demonstrate isolation using a distributed-feedback (DFB) laser chip (Fig. 5a). To maximize the on-chip pump power, we couple the DFB laser to the chip using an oxide-clad inverted taper designed to match the output mode of the laser[4]. We first characterize the isolation by coupling the DFB laser to a lensed fibre and performing a pump–probe measurement, similar to Fig. 2a. To tune the DFB laser across the ring resonance we modulate its temperature using a Peltier device and a thermistor for feedback. We observe isolation up to 13.6 dB with 65-mW input power (Fig. 5b), slightly lower than before due to the small reduction in the Q factor. We then directly butt-couple the DFB laser and isolator, and thermally lock the ring to the laser. To verify its isolation, we send pulses backwards through the device using a secondary laser, and measure their transmission (Fig. 5c,d). To ensure that the secondary laser is at the same frequency as the DFB, we mix the laser outputs on a photodiode and minimize their beat-tone.

https://doi.org/10.1038/s41566-022-01110-y

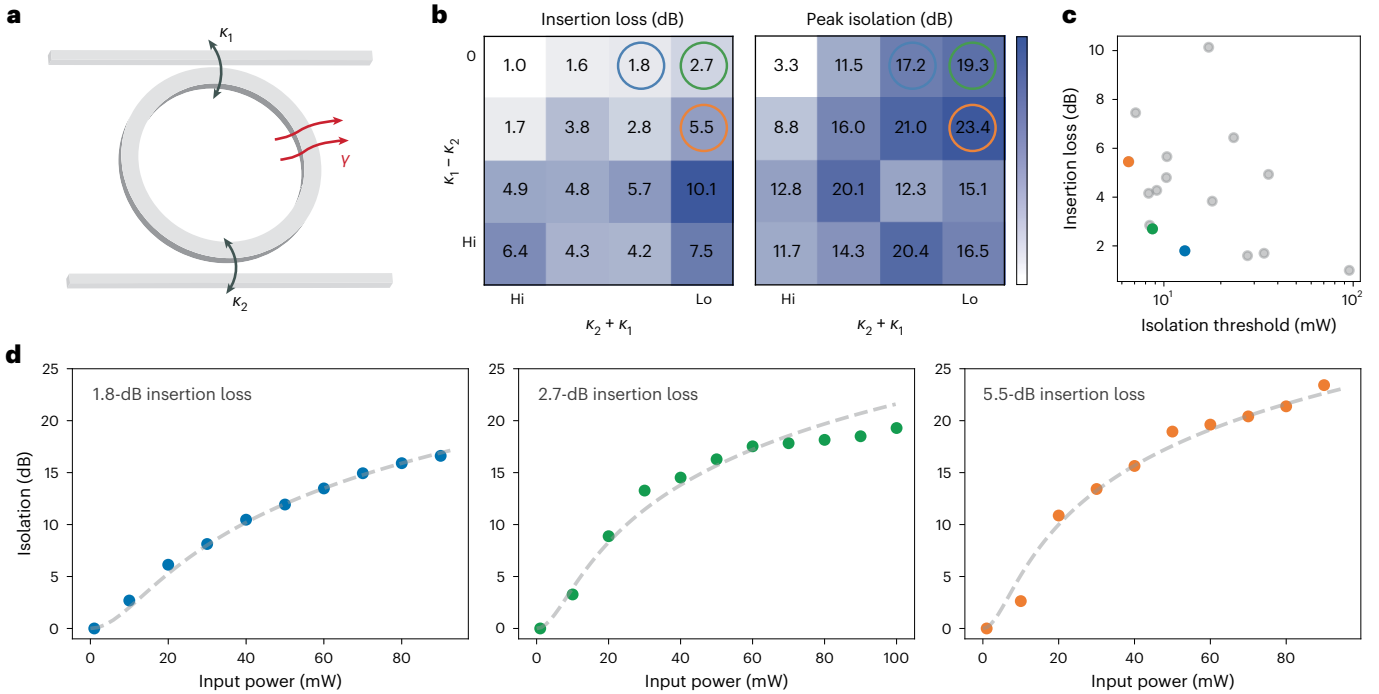

Fig. 3 | Performance optimization. a, Schematic of the isolator ring illustrating the key parameters: κ_1, κ_2 and γ—the input coupling rate, output coupling rate and intrinsic loss rate, respectively. **b**, Heatmaps showing the measured insertion loss and peak isolation for varied coupling rates κ_1 and κ_2. The colour bar limits are set by the min and max of each plot (white: 1.0-dB insertion loss, 3.3-dB peak isolation; dark blue: 10.1-dB insertion loss, 23.4-dB peak isolation). Well-performing parameters are highlighted with blue, green and orange circles. **c**, Correlations of the isolation and insertion losses from **b**. **d**, Pump-power-dependent isolation for the three highlighted rings.

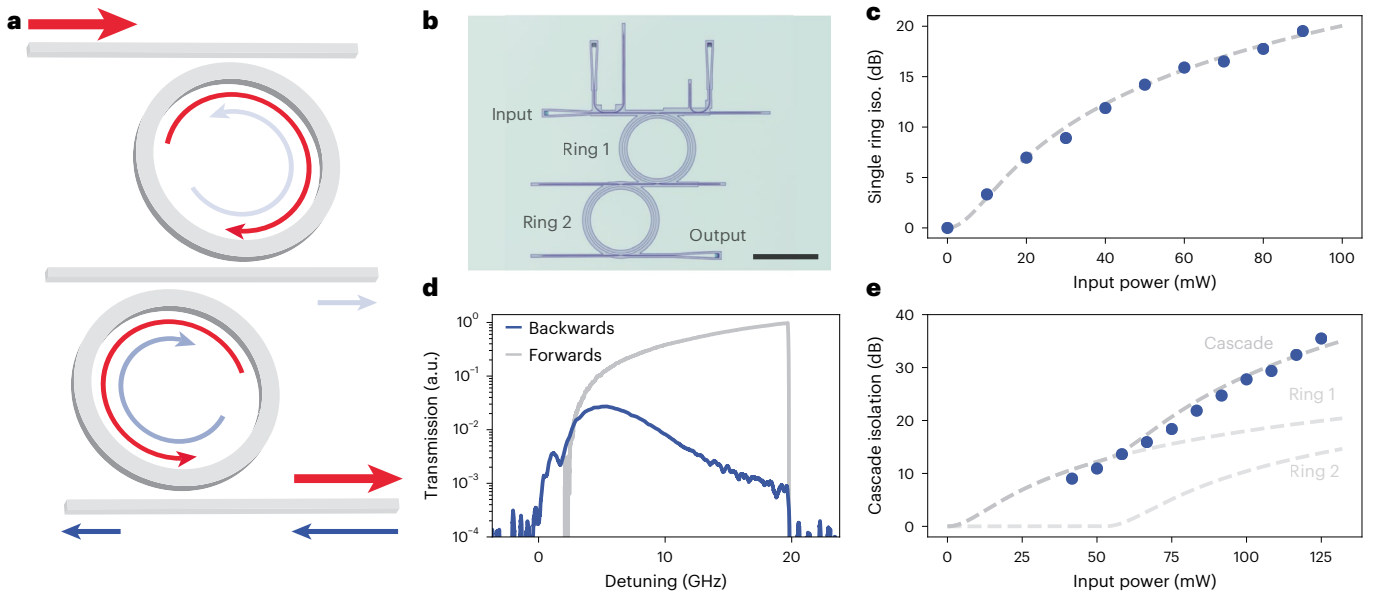

Fig. 4 | Isolator cascade. a, Schematic of cascaded isolator rings. **b**, Optical micrograph of fabricated cascaded isolator rings. Scale bar, 200 µm. **c**, Theoretical (dashed line) and experimental (blue data points) power-dependent single-ring isolation. **d**, Transmission in the forwards and backwards direction from the cascaded isolator rings with a 110-mW pump. **e**, Theoretical (dashed line) and experimental (blue data points) power-dependent isolation of cascaded rings. The theoretical fit is calculated by multiplying the isolation ratio from a single ring to a second ring redshifted from the first. Measurements start from 40 mW, as this much pump power is needed to overlap the two ring resonances.

Conclusion

We have demonstrated on-chip optical isolators utilizing the Kerr effect that are fully passive. By tuning the coupling parameters we trade off between insertion loss and isolation, demonstrating devices with an insertion loss of only 1.8 dB with 17-dB isolation, and single-ring isolation of up to 23 dB. Due to the integrated nature of these isolators, they can be easily cascaded to improve performance. By cascading two rings, we achieve 35-dB isolation with 5-dB insertion loss. Finally,

https://doi.org/10.1038/s41566-022-01110-y

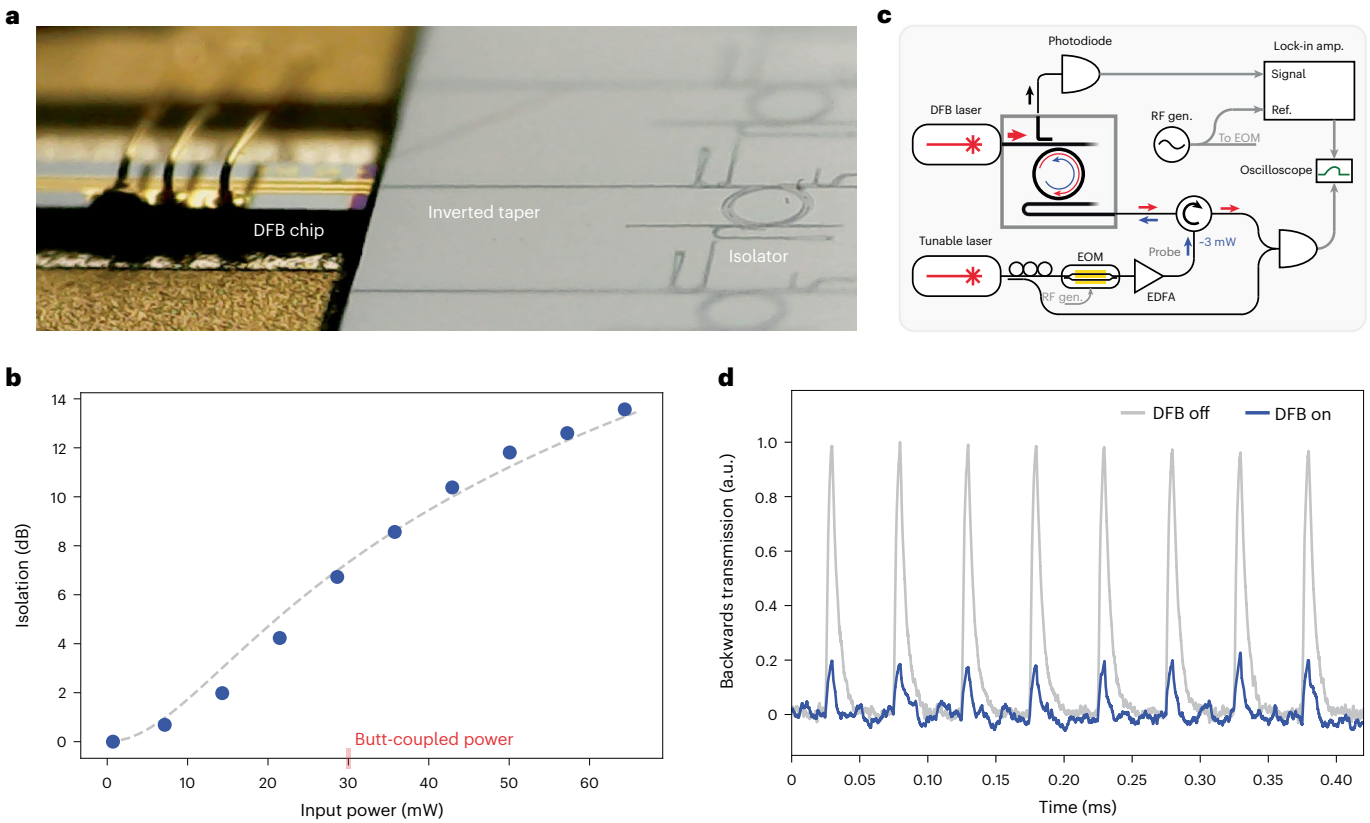

Fig. 5 | DFB hybrid integration. a, Optical image of hybrid integration of a DFB laser with the isolator. **b**, Power-dependent isolation measured with the amplified DFB laser. Blue data points show measurement and dashed line shows theoretical fit. **c**, Schematic of experimental measurement set-up for direct measurement of the hybrid integrated DFB–isolator operation. **d**, Transmission of backwards pulses with the directly coupled DFB laser on and off.

we demonstrate the application of such a device to isolate the output of an edge-coupled DFB laser chip.

As these devices are fully passive and magnet-free, they require no external drive and can operate without generating any electromagnetic interference or magnetic field background. In spite of this, their performance is still competitive with state-of-the-art active and magnetic integrated isolators (Supplementary Table 1)[11,13,15,18–20,40–42]. Furthermore, better-controlled fabrication from commercial foundries will allow for higher quality factors[43] and enable cascading of more than two rings, pushing the power threshold for 20-dB isolation down to below 2 mW and the achievable isolation to over 70 dB (Supplementary Section 10). As many hybrid and heterogeneously integrated optical systems already contain high-quality photonics in Kerr materials, this type of isolator can be immediately incorporated into state-of-the-art integrated photonics.

Online content

Any methods, additional references, Nature Portfolio reporting summaries, source data, extended data, supplementary information, acknowledgements, peer review information; details of author contributions and competing interests; and statements of data and code availability are available at https://doi.org/10.1038/s41566-022-01110-y.

References

1. Xiang, C. et al. Laser soliton microcombs heterogeneously integrated on silicon. *Science* **373**, 99–103 (2021).
2. Kippenberg, T. J., Gaeta, A. L., Lipson, M. & Gorodetsky, M. L. Dissipative Kerr solitons in optical microresonators. *Science* **361**, eaan8083 (2018).
3. de Beeck, C. O. et al. III/V-on-lithium niobate amplifiers and lasers. *Optica* **8**, 1288–1289 (2021).
4. Shen, B. et al. Integrated turnkey soliton microcombs. *Nature* **582**, 365–369 (2020).
5. Jin, W. et al. Hertz-linewidth semiconductor lasers using CMOS-ready ultra-high-Q microresonators. *Nat. Photon.* **15**, 346–353 (2021).
6. Yang, K. Y. et al. Inverse-designed multi-dimensional silicon photonic transmitters. Preprint at https://arxiv.org/abs/2103.14139 (2021).
7. Shu, H. et al. Microcomb-driven silicon photonic systems. *Nature* **605**, 457–463 (2022).
8. Liu, Y. et al. A photonic integrated circuit based erbium-doped amplifier. *Science* **376**, 1309–1313 (2022).
9. Jalas, D. et al. What is—and what is not—an optical isolator. *Nat. Photon.* **7**, 579–582 (2013).
10. Srinivasan, K. & Stadler, B. J. H. Magneto-optical materials and designs for integrated TE-and TM-mode planar waveguide isolators: a review. *Opt. Mater. Express* **8**, 3307–3318 (2018).
11. Du, Q. et al. Monolithic on-chip magneto-optical isolator with 3-dB insertion loss and 40-dB isolation ratio. *ACS Photonics* **5**, 5010–5016 (2018).
12. Bi, L. et al. On-chip optical isolation in monolithically integrated non-reciprocal optical resonators. *Nat. Photon.* **5**, 758–762 (2011).
13. Yan, W. et al. Waveguide-integrated high-performance magneto-optical isolators and circulators on silicon nitride platforms. *Optica* **7**, 1555–1562 (2020).
14. Tzuang, L. D., Fang, K., Nussenzveig, P., Fan, S. & Lipson, M. Non-reciprocal phase shift induced by an effective magnetic flux for light. *Nat. Photon.* **8**, 701–705 (2014).

15. Fang, K. et al. Generalized non-reciprocity in an optomechanical circuit via synthetic magnetism and reservoir engineering. *Nat. Phys.* **13**, 465–471 (2017).
16. Kim, J. H., Kuzyk, M. C., Han, K., Wang, H. & Bahl, G. Non-reciprocal brillouin scattering induced transparency. *Nat. Phys.* **11**, 275–280 (2015).
17. Kittlaus, E. A., Otterstrom, N. T., Kharel, P., Gertler, S. & Rakich, P. T. Non-reciprocal interband Brillouin modulation. *Nat. Photon.* **12**, 613–619 (2018).
18. Tian, H. et al. Magnetic-free silicon nitride integrated optical isolator. *Nat. Photon.* **15**, 828–836 (2021).
19. Kittlaus, E. A. et al. Electrically driven acousto-optics and broadband non-reciprocity in silicon photonics. *Nat. Photon.* **15**, 43–52 (2021).
20. Sohn, D. B., Örsel, O. E. & Bahl, G. Electrically driven optical isolation through phonon-mediated photonic autler–townes splitting. *Nat. Photon.* **15**, 822–827 (2021).
21. Sounas, D. L., Soric, J. & Alu, A. Broadband passive isolators based on coupled nonlinear resonances. *Nat. Electron.* **1**, 113–119 (2018).
22. Yang, K. Y. et al. Inverse-designed non-reciprocal pulse router for chip-based lidar. *Nat. Photon.* **14**, 369–374 (2020).
23. Hua, S. et al. Demonstration of a chip-based optical isolator with parametric amplification. *Nat. Commun.* **7**, 13657 (2016).
24. Del Bino, L. et al. Microresonator isolators and circulators based on the intrinsic nonreciprocity of the Kerr effect. *Optica* **5**, 279–282 (2018).
25. Cao, Q.-T. et al. Reconfigurable symmetry-broken laser in a symmetric microcavity. *Nat. Commun.* **11**, 1136 (2020).
26. Xuan, Y. et al. High-Q silicon nitride microresonators exhibiting low-power frequency comb initiation. *Optica* **3**, 1171–1180 (2016).
27. Wilson, D. J. et al. Integrated gallium phosphide nonlinear photonics. *Nat. Photon.* **14**, 57–62 (2020).
28. Jung, H. et al. Tantala Kerr nonlinear integrated photonics. *Optica* **8**, 811–817 (2021).
29. Lu, X., Lee, J. Y., Rogers, S. & Lin, Q. Optical Kerr nonlinearity in a high-Q silicon carbide microresonator. *Opt. Express* **22**, 30826–30832 (2014).
30. Guidry, M. A. et al. Optical parametric oscillation in silicon carbide nanophotonics. *Optica* **7**, 1139–1142 (2020).
31. Lu, J. et al. Periodically poled thin-film lithium niobate microring resonators with a second-harmonic generation efficiency of 250,000%/w. *Optica* **6**, 1455–1460 (2019).
32. Wang, C. et al. Monolithic lithium niobate photonic circuits for Kerr frequency comb generation and modulation. *Nat. Commun.* **10**, 978 (2019).
33. Shi, Y., Yu, Z. & Fan, S. Limitations of nonlinear optical isolators due to dynamic reciprocity. *Nat. Photon.* **9**, 388–392 (2015).
34. Del Bino, L., Silver, J. M., Stebbings, S. L. & Del'Haye, P. Symmetry breaking of counter-propagating light in a nonlinear resonator. *Sci. Rep.* **7**, 43142 (2017).
35. Cao, Q.-T. et al. Experimental demonstration of spontaneous chirality in a nonlinear microresonator. *Phys. Rev. Lett.* **118**, 033901 (2017).
36. Moss, D. J., Morandotti, R., Gaeta, A. L. & Lipson, M. New CMOS-compatible platforms based on silicon nitride and hydex for nonlinear optics. *Nat. Photon.* **7**, 597–607 (2013).
37. Kim, S. et al. Dispersion engineering and frequency comb generation in thin silicon nitride concentric microresonators. *Nat. Commun.* **8**, 372 (2017).
38. Gao, M. et al. Probing material absorption and optical nonlinearity of integrated photonic materials. *Nat. Commun.* **13**, 3323 (2022).
39. Padmaraju, K. & Bergman, K. Resolving the thermal challenges for silicon microring resonator devices. *Nanophotonics* **3**, 269–281 (2014).
40. Herrmann, J. F. et al. Mirror symmetric on-chip frequency circulation of light. *Nat. Photon.* **16**, 603–608 (2022).
41. Lira, H., Yu, Z., Fan, S. & Lipson, M. Electrically driven nonreciprocity induced by interband photonic transition on a silicon chip. *Phys. Rev. Lett.* **109**, 033901 (2012).
42. Dostart, N., Gevorgyan, H., Onural, D. & Popović, M. A. Optical isolation using microring modulators. *Opt. Lett.* **46**, 460–463 (2021).
43. Liu, J. et al. High-yield, wafer-scale fabrication of ultralow-loss, dispersion-engineered silicon nitride photonic circuits. *Nat. Commun.* **12**, 2236 (2021).

Methods

Device fabrication

Thin-film silicon nitride (310 nm) was deposited on a silicon dioxide/silicon carrier wafer using low-pressure chemical vapour deposition. The isolator device patterns were defined using electron-beam lithography (JEOL JBX-6300FS), using ZEP520A as the electron resist. Post development, the patterns were transferred onto silicon nitride by inductively coupled plasma etching with CHF_3/CF_4 chemistry. After the etch, the resist was removed using Piranha solution, and the silicon-nitride chips were subsequently annealed in a N_2 environment at 1,100 °C.

Isolator measurements

A scanning laser (Toptica) was split into two paths using a directional coupler. One path served as the pump and one as the probe. The pump path was passed through a polarization controller and was amplified by an erbium-doped fibre amplifier (EDFA; IPG) before being sent to the chip. The probe path was modulated using an EOM (Optilab), passed through a polarization controller, and amplified by an EDFA (Thorlabs) before being sent to the chip. The backwards transmission was measured using a photodiode (Thorlabs), a lock-in amplifier (Stanford Instruments) and an oscilloscope (Rigol). Inverse-designed grating couplers optimized for transmission at 1,550 nm were used to couple to and from the chip. To minimize leakage from the probe input fibre to the detection fibre, the grating inputs were oriented perpendicular to each other. For fixed and scanning measurements of power-dependent isolation, the EOM was modulated with a 90-kHz signal from an arbitrary waveform generator (Rigol) and the same signal was used for lock-in detection. For frequency-dependent measurements, the EOM was driven by an amplified (Minicircuits) 90-kHz lock-in signal mixed (Minicircuits) with a high-frequency modulation from a frequency synthesizer (Rohde and Schwarz).

DFB operation

The DFB laser was driven by a precision source (Keithley) with 380-mW electrical power. To thermally stabilize and tune the frequency of the laser, the laser mount was cooled by a Peltier device using a 10-kΩ thermistor to provide feedback control with a temperature controller (Thorlabs).

Data availability

All data are available from the corresponding authors upon reasonable request.

Acknowledgements

We thank D. Carlson, T. Briles, J. Zang, J. Black, S.-P. Yu, F. M. Mayor, J. F. Herrmann, A. H. Safavi-Naeini, S. Papp and R. Trivedi for collaboration and discussions, and L. Wu and K. Vahala for assistance with the DFB laser. A.W. acknowledges the Herb and Jane Dwight Stanford Graduate Fellowship (SGF) and the NTT Research Fellowship for support. G.H.A. acknowledges support from STMicroelectronics Stanford Graduate Fellowship (SGF) and Kwanjeong Educational Foundation. K.V.G. acknowledges support from the Research Foundation – Flanders (FWO) (12ZB520N). The authors from Stanford acknowledge funding support from DARPA under the LUMOS programme. Part of this work was performed at the Stanford Nano Shared Facilities (SNSF)/Stanford Nanofabrication Facility (SNF), supported by the National Science Foundation under award no. ECCS-2026822.

Author contributions

A.D.W., G.H.A., K.V.G. and K.Y.Y. conceived of the project. A.D.W., G.H.A. and K.V.G. performed the experiments. G.H.A. developed the silicon-nitride fabrication process and fabricated the devices. L.C. and J.E.B. provided the semiconductor laser chip and experimental guidance. J.V. supervised the project. All authors contributed to data analysis and writing of the manuscript.

Competing interests

The authors declare no competing interests.

Additional information

Supplementary information The online version contains supplementary material available at https://doi.org/10.1038/s41566-022-01110-y.

Correspondence and requests for materials should be addressed to Alexander D. White or Geun Ho Ahn.

Peer review information *Nature Photonics* thanks Sunil Mittal and the other, anonymous, reviewer(s) for their contribution to the peer review of this work.